

Article

Modes of Occurrence of Critical Metal Elements (Li, REEs and Other Critical Elements) in Low-Grade Bauxite from Southern Shanxi Province, China

Shangqing Zhang ¹, Fenghua Zhao ^{1,*}, Dongna Liu ² , Lei Zhao ¹, Xiaohui Zhang ², Junwei Lin ² , Haiyu Dong ², Shuang Zhao ¹, Xuefei Liu ³ and Minjie Zan ⁴

¹ College of Geoscience and Survey Engineering, China University of Mining and Technology (Beijing), Beijing 100083, China

² College of Mining Engineering, Taiyuan University of Technology, Taiyuan 030024, China

³ State Key Laboratory of Geological Processes and Mineral Resources, China University of Geosciences, Beijing 100083, China

⁴ China Testing & Certification International Group Beijing Technology Co., Ltd., Beijing 101102, China

* Correspondence: zfh@cumtb.edu.cn

Abstract: The low-grade bauxite in southern Shanxi Province, China is enriched in multiple critical metal elements, including Li, Ga, V, Se, and rare earth elements (REEs), which have reached the standard of comprehensive utilization as independent deposits or associated resources. Even more importantly, identifying the modes of occurrence of these critical elements is essential for designing technologies to extract critical metals from bauxite ores. This study used a combination of direct (X-ray diffraction, scanning electron microscopy–energy dispersive X-ray spectroscopy, and micro-X-ray fluorescence spectrometer), and indirect (size sieving method, float-sink experiment, and correlation analysis) methods to effectively reveal the distribution of critical elements in the different identified mineral phases. The results regarding the low-grade bauxite are as follows: Li was mainly hosted in cookeite as an independent mineral; Ga was mainly associated with diaspore; anatase is the main carrier mineral for V; REEs were present in the low-grade bauxite in multiples modes of occurrence, the most common of which were goyazite, and to a lesser extent, florencite; Se primarily occurs in sulfides. This study contributes to the development and utilization of these essential metal resources in bauxite by providing a useful reference.

Keywords: modes of occurrence; critical metal elements; low-grade bauxite; indirect and direct methods; cookeite



Citation: Zhang, S.; Zhao, F.; Liu, D.; Zhao, L.; Zhang, X.; Lin, J.; Dong, H.; Zhao, S.; Liu, X.; Zan, M. Modes of Occurrence of Critical Metal Elements (Li, REEs and Other Critical Elements) in Low-Grade Bauxite from Southern Shanxi Province, China. *Minerals* **2022**, *12*, 990. <https://doi.org/10.3390/min12080990>

Academic Editor: Giovanni Mongelli

Received: 19 July 2022

Accepted: 2 August 2022

Published: 4 August 2022

Publisher's Note: MDPI stays neutral with regard to jurisdictional claims in published maps and institutional affiliations.



Copyright: © 2022 by the authors. Licensee MDPI, Basel, Switzerland. This article is an open access article distributed under the terms and conditions of the Creative Commons Attribution (CC BY) license (<https://creativecommons.org/licenses/by/4.0/>).

1. Introduction

Critical metals play a pivotal role in new energy, new materials, aerospace, national defense, and electronic technology. Some governments, such as the European Union, Russia, the United States, and Australia, have adopted critical metal development policies to maintain the security of essential metal supply chains [1–3]. The European Commission's recent list of critical metal resources mainly involves REEs, Sc, V, Co, Ga, Sr, Nb, Hf, and Ta [2]. Bauxite and bauxite residue are substantially enriched of these critical metals [4].

Determining the modes of occurrence of critical metal elements in bauxite is crucial for designing the technology required to extract them and for studying the enrichment mechanism. Analytical methods for determining modes of occurrence of critical elements can be divided into two categories based on their characteristics: indirect and direct methods [5,6]. The indirect method includes statistical analysis, the size sieving method, float-sink experiment, and selective leaching techniques. Correlation and R-mode principal component analysis have shown that REEs are present as independent minerals in the weathering profiles of Devonian bauxite from central Russia in the form of carnallite, goyazite, and svanbergite–woodhouseite [7]. Univariate and multivariate statistics conclude that Al-, Fe-,

and Ti-oxi-hydroxides control the distribution of most critical metals in Cretaceous karst bauxite from central and southern Italy [8]. Selective leaching techniques were used by Zhang et al. (2019) [9] on bauxite from central Guizhou Province, China, and showed that Li is hosted mainly in clay minerals, with minor amounts in diaspore and boehmite.

Direct methods have also been commonly used to study modes of occurrence of elements, including optical microscopy, electron microprobe analysis–wavelength dispersive X-ray spectrometers (EMPA–WDS), scanning electron microscopy–energy-dispersive X-ray spectroscopy (SEM–EDS), laser ablation–inductively coupled plasma mass spectrometer (LA–ICP–MS), and Micro X-ray fluorescence spectrometer (μ XRF). EPMA was used to observe independent REE minerals in Permian bauxite from western Guangxi, southwest China [10]. Using SEM–EDS, Zhu et al. (2019) [11] found that most LREEs were adsorbed as ions on the surfaces of clay minerals and diaspore, while HREEs were hosted in xenotime in the Songqi karstic bauxite from northern China. The Greek bauxite and bauxite residue were analyzed by LA–ICP–MS, and high Sc concentrations in hematite was found. [12]. Similarly, Ling et al. (2020) [13] employed LA–ICP–MS to study karst bauxite in central Guizhou Province, China, and discovered that montmorillonite is the main carrier mineral for Li, and REEs are mainly found in monazite.

Although Shanxi Province holds the majority of China’s bauxite resources [14], little research has been conducted on the modes of occurrence of essential metal elements in Shanxi bauxite. The bauxite deposits from southern Shanxi Province, North China have been found to be enriched in a variety of critical elements [15], suggesting that they may be exploited and utilized. In this study, selected low-grade bauxite ore was comprehensively analyzed using indirect and direct methods to identify the modes of occurrence of critical elements including Li, Ga, V, Se, and REEs, eventually providing a valuable reference for the development and utilization of these critical metal resources.

2. Materials and Methods

The Shanxi bauxite deposits are hosted in the lower member of Carboniferous Benxi Formation, which is unconformably underlain by the Middle Ordovician carbonate. A bulk bauxite ore sample was collected from fresh outcrops in the bauxite mine of the Yuncheng area, southern Shanxi Province, North China (Figure 1).

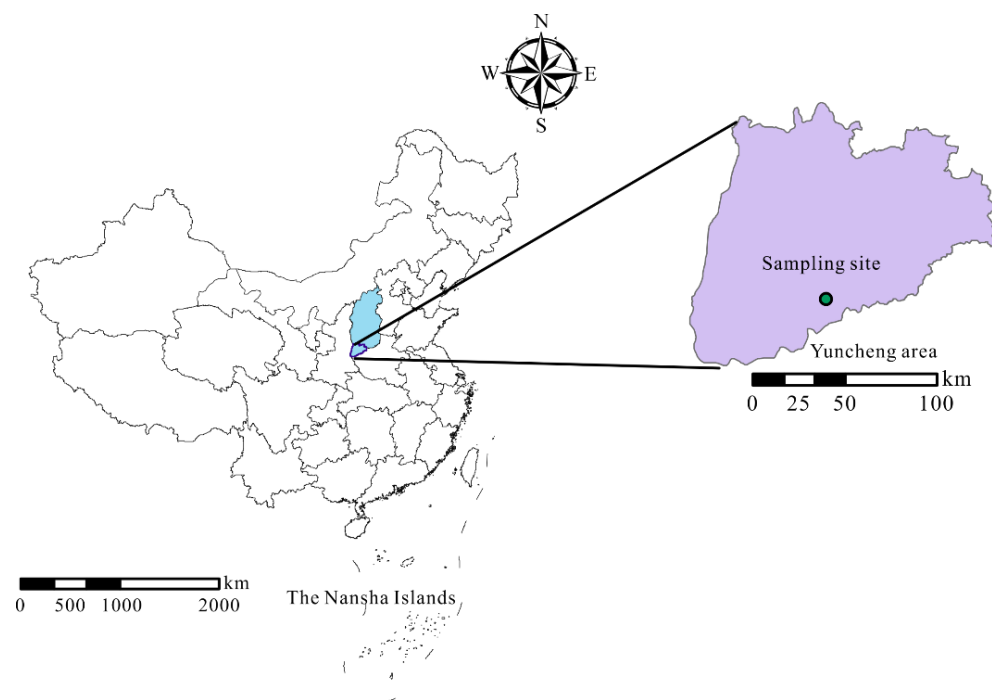


Figure 1. Locality map showing the sampling site in the Yuncheng area, Shanxi Province.

The bulk bauxite ore sample (Y1) was crushed to <1 mm in size. The crushed samples were sieved through sieve apertures of 1, 0.5, 0.25, 0.125, 0.074, and 0.044 mm. Mechanically shaken samples with particle sizes of $-1 + 0.5$, $-0.5 + 0.25$, and $-0.25 + 0.125$ mm were analyzed, while others were analyzed using the wet sieve. Three particle size samples of $-1 + 0.5$, $-0.5 + 0.25$, and $-0.25 + 0.125$ mm were used for the float-sink experiment. To make heavy liquids with densities of 1.60 g/cm^3 and 2.65 g/cm^3 , carbon tetrachloride and tribromomethane were chosen. Then, nine samples of three density fractions were finally obtained according to GB/T 478-2008 [16]. Finally, these dried samples were ground to <0.074 mm for mineralogical and geochemical analysis.

The Sample Y1 was determined by the Rietveld method using a X-ray powder diffractometer (SmartLab, Rigaku, Tokyo, Japan) equipped with Cu-K α radiation operated at 40 kV and 200 mA. The XRD pattern was recorded over a 2θ interval of $2-90^\circ$, with a step size of 0.02° and a count time of 3.0 s per step. The samples subjected to size and density fractionation were determined by XRD using a Rigaku (Tokyo, Japan) D/max-2500PC diffractometer equipped with Cu-K α radiation operated at 40 kV and 100 mA. All XRD patterns were collected using the continuous sweep method from 3° to 70° (2θ) with a scanning speed of 4° per minute. The diffractograms were processed using the JADE 6.5 software (Materials Data, Livermore, CA, USA) and the Rietveld-based SiroquantTM software (V4, Canberra, Australia) [17]. The mineralogical analysis results are shown in Table 1. For clay-mineral identification, oriented-aggregates of the <2 μm clay fractions from the raw ore sample were evaluated by XRD according to SY/T5163-2018 [18].

Table 1. Quantitative mineralogical compositions (%) of sample Y1 and the samples subjected to size and density fractionation.

Sample	Size mm	Density g/cm^3	Diaspore	Anatase	Goyazite	Cookeite	Kaolinite
Y1			37.9	2.7	3.5	30.7	25.2
L1	$-1 + 0.5$		23.5	1	4	38.8	32.8
L2	$-0.5 + 0.25$		23.7	1.2	3.8	38.9	32.4
L3	$-0.25 + 0.125$		24.5	1.3	4.1	34.7	35.5
L4	$-0.125 + 0.074$		26.3	1.5	4.2	34.9	33
L5	$-0.074 + 0.044$		28.1	1.4	3.3	31	36.2
L6	-0.044		26.9	1.8	3.4	31.9	36
L1-1		<1.60	-	-	-	-	-
L1-2	$-1 + 0.5$	1.60–2.65	22.7	0.9	4.4	38.5	33.4
L1-3		>2.65	36.7	0.9	2.8	34	25.6
L2-1		<1.60	-	-	-	-	-
L2-2	$-0.5 + 0.25$	1.60–2.65	24.4	1.4	4.5	33.5	36.1
L2-3		>2.65	40.1	0.9	2.2	33.1	23.9
L3-1		<1.60	-	-	-	-	-
L3-2	$-0.25 + 0.125$	1.60–2.65	23.7	1.5	4.7	35	35
L3-3		>2.65	31.4	1	2.5	35.3	29.9

X-ray fluorescence spectrometer (XRF, PANalytical-PW2424, Malvern Panalytical, Malvern, UK) was used to determine the major elements of the sample Y1. Loss on ignition (LOI; 36.97 wt.%) was determined using the gravimetric method. After digestion of all powder samples, major and trace elements were analyzed using inductively coupled plasma emission spectrometry (ICP-AES, Agilent-5110, Agilent, Santa Clara, CA, USA) and inductively coupled plasma mass spectrometry (ICP-MS, Agilent-7900, Agilent, Santa Clara, CA, USA) with accuracies better than 10%. Specific analytical methods were described by Franzini et al. (1972) [19] and Qi et al. (2000) [20]. The chemical analysis results are shown in Supplementary Table S1.

Before the raw bauxite sample was subjected to size and density fractionation, representative samples were polished to make thin sections for optical, SEM-EDS, and μXRF analysis. Polished sections of bauxite samples that were coated by C were also stud-

ied using a Leica DM4500P (Leica, Wetzlar, Germany) polarizing microscope and a field emission-scanning electron microscope (SU5000, Hitachi, Tokyo, Japan) equipped with an energy dispersive spectrometer system and backscattered electron probe HHTNT-511-9022 (Hitachi, Tokyo, Japan) and Quantax Compact30 (Bruker, Billerica, MA, USA), respectively.

The Micro X-ray fluorescence spectrometer (Bruker M4 TORNADO, Bruker, Billerica, MA, USA) has two large-area silicon drift detectors with a super light window and a specially tuned Rh X-ray tube, which can analyze almost all elements from Na (11) to U (92). A poly-capillary optics can perform a rapid, in situ, and non-destructive μ XRF analysis on the polished bauxite ore sample to obtain semi-quantitative chemical data at a spatial resolution of 20 μ m [21]. In this experiment, the 65.7 mm \times 55.8 mm sample area was selected on an internal camera in the chamber under vacuum (vacuum of 20 mbar). Micro μ XRF experiments lasted 27 h with an X-ray tube energy of 50 kV, an operating current of 600 mA, a 10 ms per pixel spectrum acquisition time, a minimum integration time of 0.3 ms at a single point, and a pixel step-size of 20 μ m. The intensity of the X-ray spectrum for all the scanning element mapping is proportional to the pixel intensity that gridded two-dimensional element distribution maps. The scanning elemental maps on the bauxite sample were processed using the HyperMap software provided by Bruker Micro Analytics.

3. Results

3.1. Mineral Characterization

Quantitative mineralogical compositions reveal that the minerals in the sample Y1 are mainly composed of diaspore, cookeite, and kaolinite, with minor amounts of anatase and goyazite (Figure 2a, Table 1), of which the identification of cookeite is discussed below. Optical microscope images show that the sample consists of diaspore, argillaceous minerals, and carbonized plant debris (Figure 3a,b). Diaspore was commonly in the form of clastic aggregates with a maximum particle size of around 0.1 mm. The clay minerals were predominantly cryptocrystalline, with opaque-translucent minerals and diaspore interspersed throughout. The abundant plant debris and fusinite interlocked with diaspore and clays as pore and cell fracture fillings, which were pile-like aggregates. SEM-EDS analysis revealed trace amounts of illite and zircon (Figure 3), but they did not show up in the XRD pattern because they were below the detection limit of XRD [22]. In cell cavities, the diaspore coexisted with scale-like aggregates of kaolinite (Figure 3c–e). Some diaspores were highly crystalline, penetrating the clay minerals in long columns (Figure 3c,d), and co-filling the cell cavities with the latter, while a minor proportion coexists with quartz (Figure 3h).

The mineral species in different size samples did not change after sieving, as shown in Table 1, but the crushing process affected the amount of different minerals. The size sieving experiment had the greatest impact on cookeite, and its amount decreased as particle size decreased, with about 7% more cookeite in sample L1 than in sample L6. Diaspore and kaolinite mainly occurred in the particle sizes of the small sample (<0.125 mm), while goyazite and anatase amounts varied less across particle size samples.

The organic matter causes a broad hump at 20°–30° 2 θ in the less than 1.60 g/cm³ density-fractionated samples, indicating that the float-sink method efficiently separated the enriched organic matter samples (Figure 2b). Additionally, XRD patterns indicate that a few fine-grained minerals were mixed in with the enriched organic matter samples. Except for cookeite, the float-sink method demonstrates that heavy fluids with specific gravities of 2.65 g/cm³ may efficiently separate the other four minerals—i.e., kaolinite, anatase, diaspore, and goyazite (Table 1, Figure 4a). Cookeite was more equally distributed in the density-fractionated samples with densities of 1.60–2.65 g/cm³ and >2.65 g/cm³. Diaspore was particularly abundant in the >2.65 g/cm³ density-fractionated samples, while kaolinite, goyazite, and anatase were notably numerous in the 1.60–2.65 g/cm³ density-fractionated samples.

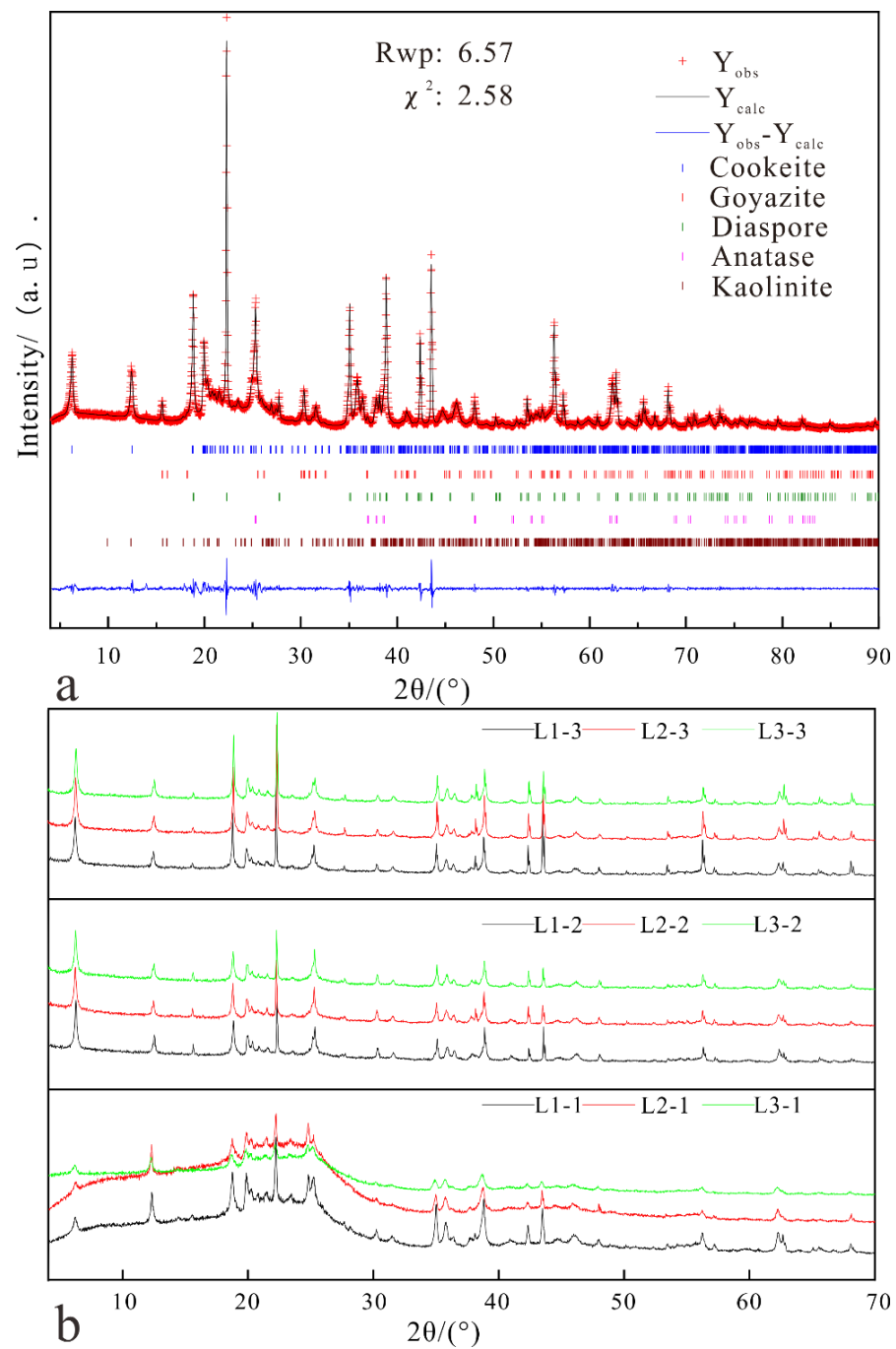


Figure 2. XRD patterns of the sample Y1 refining the mineral cell parameters using Rietveld refinement (a) and density-fractionated samples (b). Y_{obs} : observed value, Y_{calc} : calculated value.

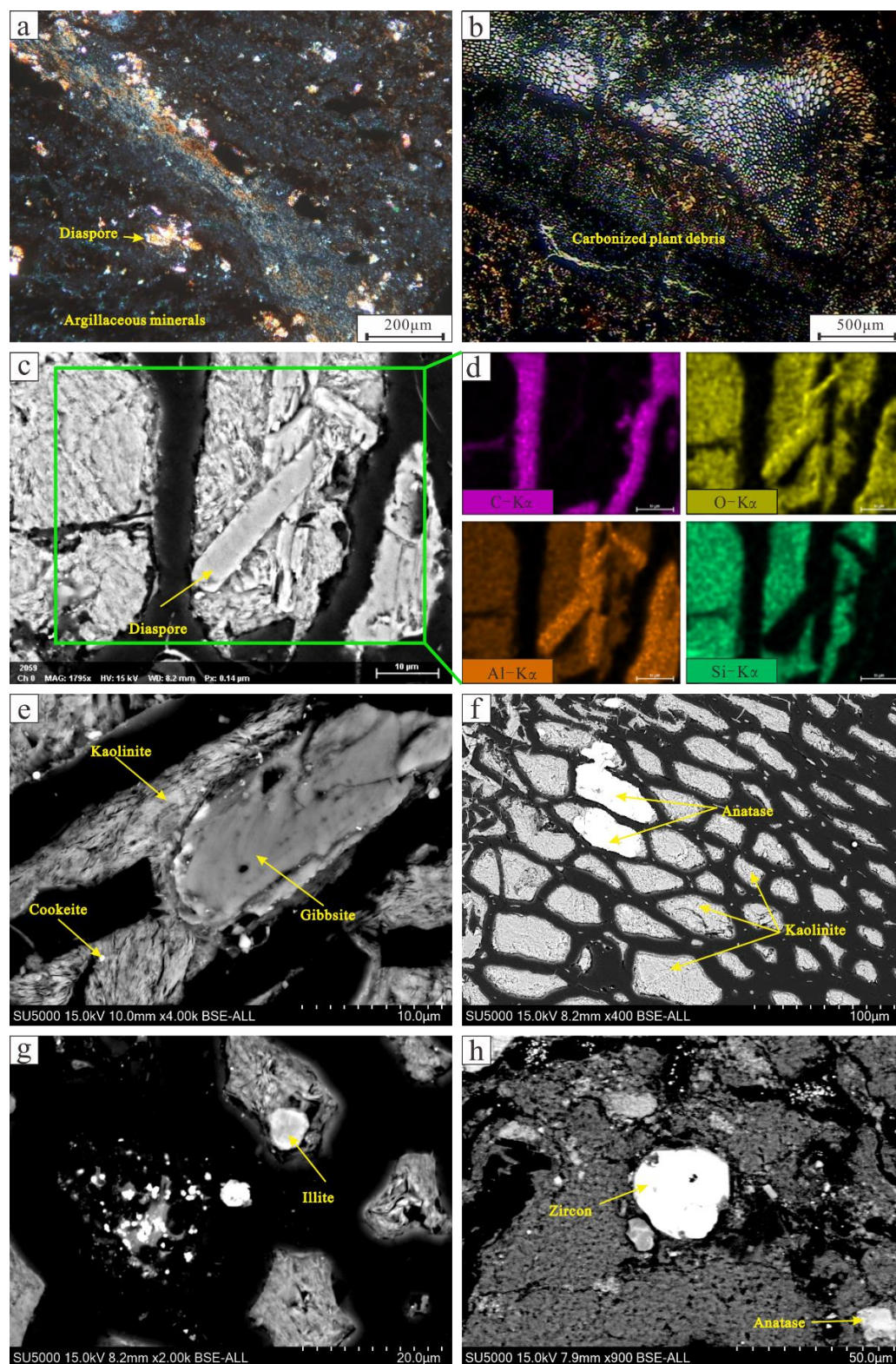


Figure 3. Optical microscope and SEM back-scattered electron images of representative samples. (a) Coexistence of diaspore and argillaceous minerals; (b) Different types of minerals filled in cell cavities of plant debris; (c) Elemental maps of C, O, Al, and Si obtained by SEM-based EDS microanalysis; (d) Enlargement of marked area in (c); (e) Kaolinite coexisting with gibbsite, and cookeite disseminated in kaolinite in granular form; (f) Cell cavities largely filled with anatase and kaolinite; (g) Illite in granular form; (h) Coexistence of well psepchicity zircon. EDS data are as in the Supplementary Table S2.

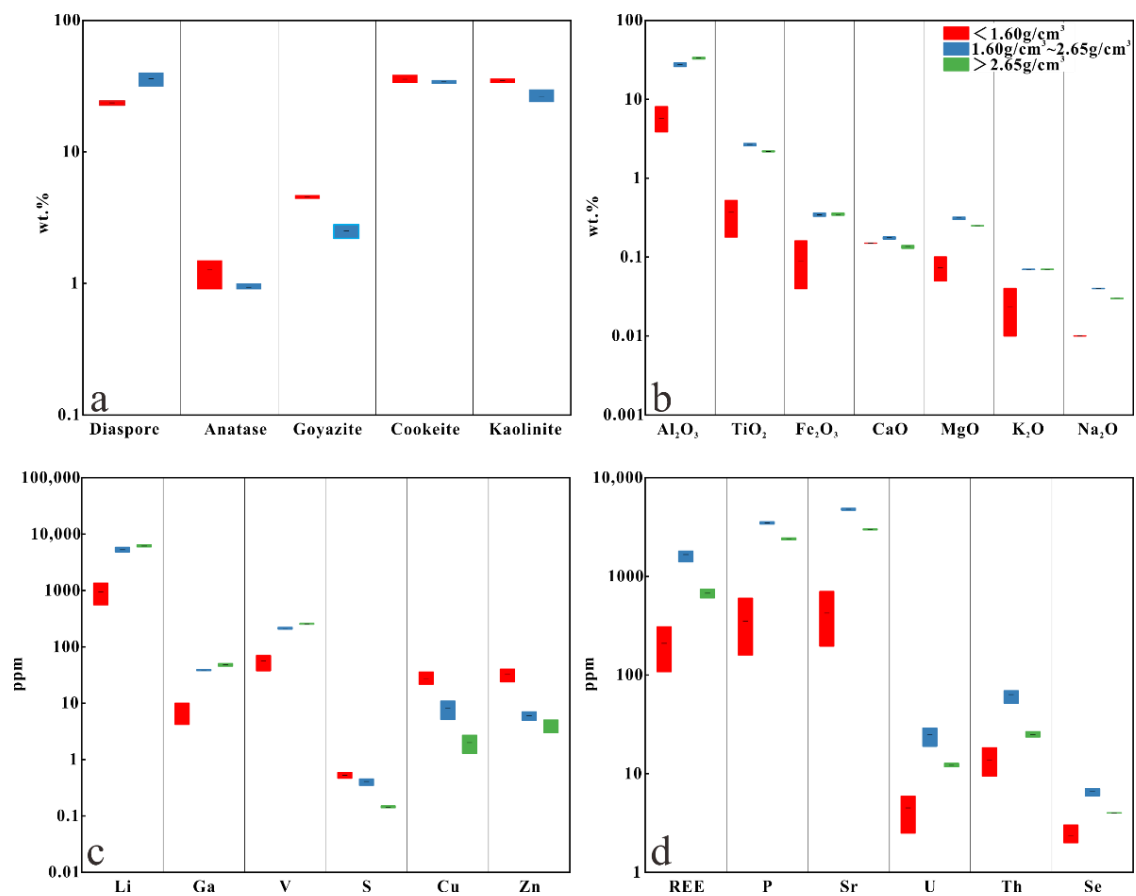


Figure 4. Box-and-whisker plots showing the mineral distribution patterns in the density-fractionated samples (a); distribution patterns of major elements in the density-fractionated samples (b); distribution patterns of trace element in the density-fractionated samples (c,d).

3.2. Chemical Characterization

3.2.1. Major Element Characterization

The sum of major elements Al_2O_3 , SiO_2 , TiO_2 , and LOI is up to 96.94 wt% in the raw sample Y1, with comparatively low Fe_2O_3 (0.28 wt%), CaO (0.12 wt%), MgO (0.31 wt%), K_2O (0.09 wt%), Na_2O (0.05 wt%), and P_2O_5 (0.48 wt%). The sample Y1 has an Al_2O_3 to SiO_2 ratio of 2.34, which exceeds the cut-off grade for bauxite ore [23].

The distribution characteristics of major elements in the size-fractionated samples (Supplementary Table S1) show that the Al_2O_3 content decreased with decreasing particle size; TiO_2 had the lowest content in the smallest sample L6, while the remaining samples were evenly distributed; the smallest sample L6 had the highest Fe_2O_3 content, while the other samples were equally distributed. The contents of CaO, MgO, K_2O , and Na_2O were equally distributed among samples of various particle sizes, which were not affected by the size sieving process.

In the L1, L2, and L3 samples, the distribution of major elements in the density fractions of light ($< 1.60 \text{ g/cm}^3$), medium ($1.60\text{--}2.65 \text{ g/cm}^3$), and heavy ($> 2.65 \text{ g/cm}^3$) were studied (Figure 4b). The Al_2O_3 contents increased as the density of the heavy fluid increased; the contents of TiO_2 , MgO, and Na_2O were highest in the medium density fractions; Fe_2O_3 and K_2O were equally distributed in the medium and heavy density fractions. In addition to CaO contents, the light density fraction has much lower levels of other main elements than that of the medium and heavy density fractions. CaO was approximately equally distributed in the three density fractions.

The positional distribution of elements Al, Fe, and Si was shown to complement existing relationships with elements Ca, S, and Cu using the μXRF imaging technique

(Figure 5). Another intriguing observation is that the Ca distribution character matched the morphology of plant debris as seen through an optical microscope. This is supported by the fact that Ca is relatively enriched in the light density fractions, implying that the proportions of Ca content were most likely associated with organic matters.

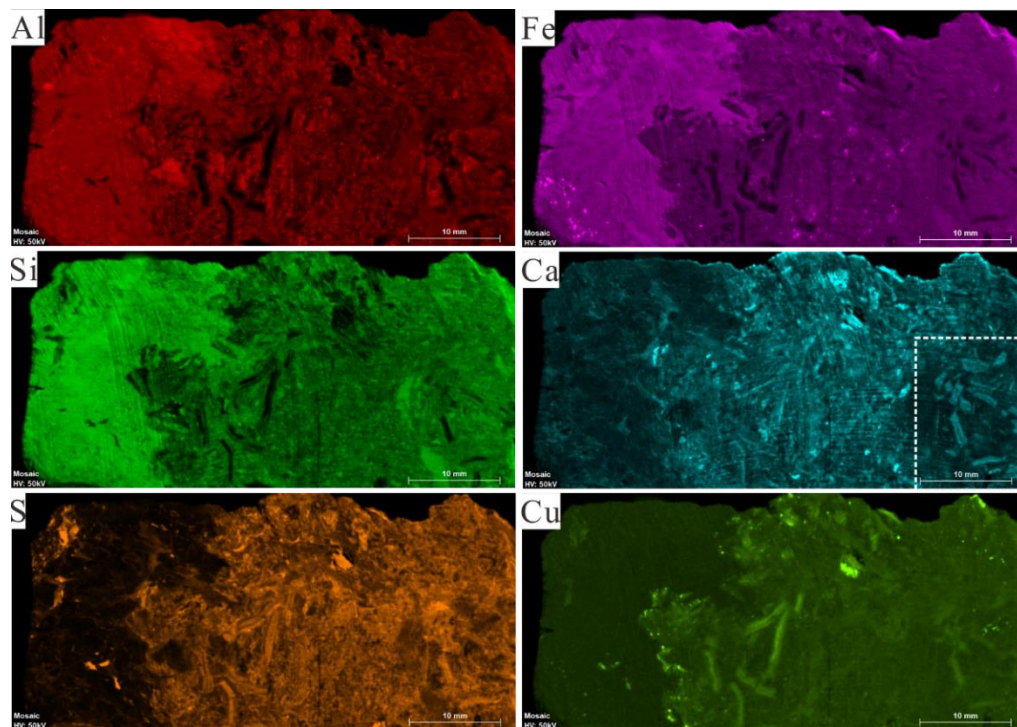


Figure 5. Elemental maps of Al, Fe, Si, Ca, S, and Cu in the sample Y1 obtained by the scanning μ XRF mapping technique. White boxed pieces appear to be obviously plant debris.

3.2.2. Trace Element Characterization

Concentration coefficients (CC, ratio of elemental concentration in investigated sample vs. the upper continental crust (UCC)) of trace elements in the low-grade bauxite ore (Y1) are shown in Figure 6. The trace elements in the sample Y1 showed large variations compared to the average composition of the UCC. The sample was abnormally enriched in Li and Se ($CC \geq 200$); it was highly enriched in Bi, Sb, and LREE ($10 \leq CC < 200$); it was moderately enriched in Sr, U, In, Ag, and Sn ($5 \leq CC < 10$); and it was slightly enriched in Ga, Sc, V, Cr, Hf, Bs, Th, Pb, As, Mo, MREE, and HREE ($2 \leq CC < 5$). The sample was relatively depleted in Co, Rb, Cs, Ba, Tl, Zn, Ge, and Re ($CC < 0.5$).

The contents of Li, Ga, V, P, and Sr increased with the increase of particle size samples after the size sieving method; the maximum contents of REEs, Th, and U were detected in sample L3; Se was equally enriched in the samples of various particle sizes. In comparison to the size-fractionated samples, sample L6 was substantially enriched in S, Cu, and Zn.

Figure 4c,d shows the contents of selected trace elements in the density-fractionated samples. The contents of P, Sr, Th, U, REY, and Se were notably elevated in medium density fractions ($1.60\text{--}2.65\text{ g/cm}^3$), followed by the heavy density fractions ($>2.65\text{ g/cm}^3$), and the last is in the light density fractions ($<1.60\text{ g/cm}^3$). The contents of Li, Ga, and V in the light, medium, and heavy density-fractionated samples successively increased, while S, Cu, and Zn contents had the opposite trend. Moreover, the μ XRF positional distribution of S and Cu mapping images was highly consistent with the Ca mapping image, which further indicates that these elements were associated with organic matter (Figure 5).

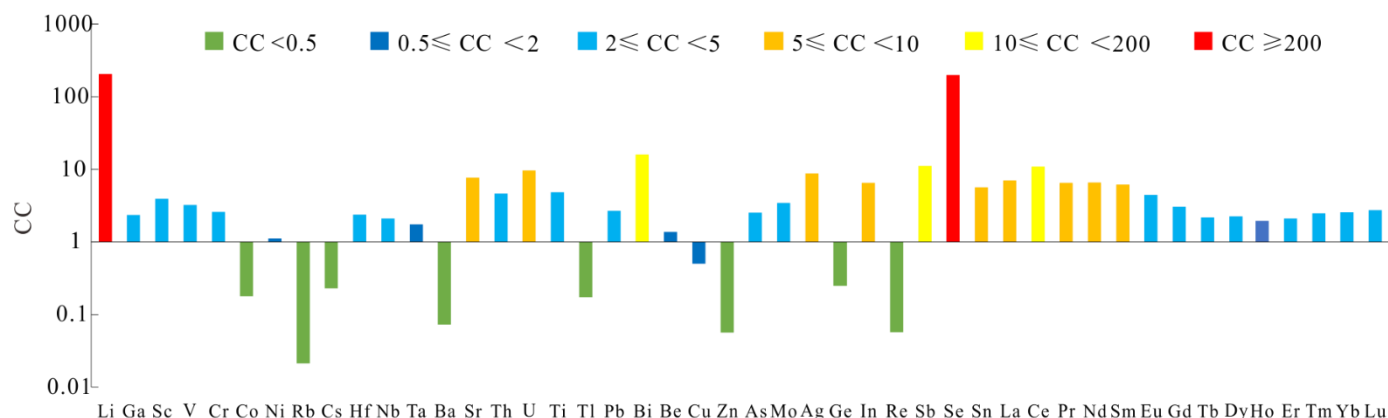


Figure 6. Concentration coefficient (CC) of trace elements in the sample Y1 from southern Shanxi Province. Data of UCC are from Taylor and McLennan (1985) [24]. CC represent ratio of elemental content in investigated bauxite vs. the UCC. Light REEs (LREE-La, Ce, Pr, Nd, and Sm), Medium REEs (MREE-Eu, Gd, Tb, and Dy), and Heavy REEs (HREE-Ho, Er, Tm, Yb, and Lu).

4. Discussion

4.1. Modes of Occurrence of Li in Low-Grade Bauxite

Critical metal Li is the core raw material for the development of the new energy industry. Li resources in karst bauxite have attracted much attention in recent years, due to the discovery of the Li super-enrichment in numerous karstic bauxite deposit regions [25–27]. It should be mentioned that a super-large Li deposit with 340,000 tons of potential Li resources is present in the karstic bauxite-bearing sequences, central Yunnan Province, China and that these Li resources are intimately associated with clay minerals [25]. Despite the fact that Shanxi Province possesses the most karstic bauxite resources in China [14], little research has been conducted on the Li and its occurrence in the Shanxi karstic bauxite deposit. In this study, the Li_2O content in the sample Y1 from southern Shanxi is up to 0.89 wt.%, which is much higher than the comprehensive utilization index of the Li element in bauxite ($\text{Li}_2\text{O} \geq 0.05\%$; [27,28]). Among the size-fractionated samples, sample L1 with a particle size of $-1 + 0.5$ mm had the highest Li_2O content (1.28 wt.%). Heavy density fractions were enriched in Li using the float-sink method, with sample L3-3 having the highest Li_2O content (1.38 wt.%).

The XRD trace of the clay fraction shows that sample Y1 contained kaolinite and cookeite (Figure 7). After being heated (450 °C) for 2.5 h, the 002 basal reflection of cookeite shifted from 6.16° to 6.40° and became more intense and widened. Cookeite has a typical structure that is characterized by the transition from dioctahedral to trioctahedral [29], where the intensity of the 002 basal reflection is significantly higher than that of the 004 basal reflection (Figures 2a and 7).

Li, as an ultra-light element, cannot be detected by SEM-EDS or μXRF . However, we can distinguish between kaolinite and cookeite by comparing their elemental composition. According to the chemical formulas of kaolinite and cookeite, these two minerals have two characteristics in EDS analysis: one is that only Al, Si, and O are displayed in the EDS analysis; the other is that the cookeite has a greater Al/Si atom ratio ($\text{Al/Si} = 1:1.66$) than kaolinite ($\text{Al/Si} = 1:1$). EDS analyses show that the Al/Si atomic ratios of cookeite in this study all ranged from 1.2 to 1.4, which was consistent with that of cookeite in the Jincheng Basin, which was described in the research of Shanxi by Zhao et al. [30]. Furthermore, high-magnification SEM images show that the cookeite morphology is mainly characterized by irregular flakiness and rarely exhibits platy morphologies (Figure 8a–d), whereas the kaolinite morphology is mostly characterized by a regular tabular shape (Figure 8d).

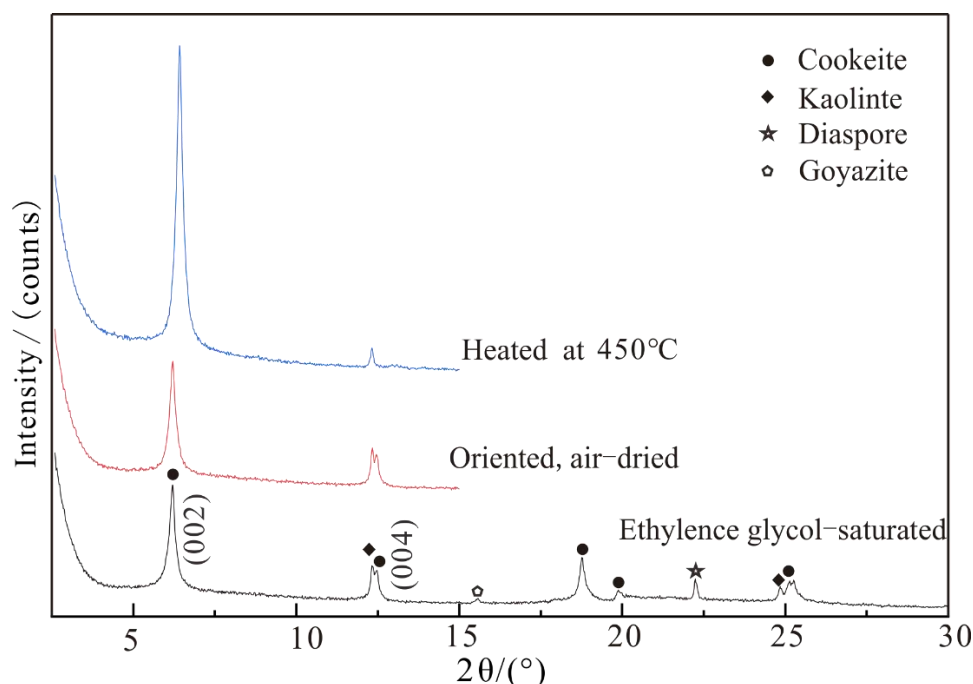


Figure 7. Oriented-aggregate XRD patterns of the sample Y1 obtained from air-dried, glycol-saturated, and heated (450 °C for 2.5 h) < 2 μm fractions.

Figure 9a,b shows the relationship between Li contents and the proportion of cookeite and kaolinite in the low-grade bauxite. As mentioned earlier, considering the significant differences in sorting different minerals between size sieving and float-sink techniques, we need to choose the appropriate sample type for correlation analysis. Li content is positively correlated with cookeite in size-fractionated samples ($r = 0.84$), but negatively correlated with kaolinite in the density-fractionated samples ($r = -0.71$), which further suggests that Li is mainly hosted in cookeite and is unrelated to kaolinite.

4.2. Modes of Occurrence of Ga and V in Low-Grade Bauxite

Ga and V are critical metals that can be successfully recycled from by-products of Al production [31,32]. Gallium extracted from alumina industrial production supplies about 90% of the world's demand [33]. The content of Ga and V in the sample Y1 is 39.3 and 195 μg/g, respectively. Among the size-fractionated samples, sample L1 with a particle size of $-1 + 0.5$ mm yielded the highest content of Ga and V (40.8 and 231 μg/g, respectively). The float-sink method shows the content of Ga and V were notably elevated in the heavy density fractions, with the sample L3-3 having the maximum content of Ga and V (50.7 and 258 μg/g, respectively).

The fact that Ga^{3+} (0.62 nm) and Al^{3+} (0.57 nm) have similar ionic radii and can be easily isomorphous meant that results could be substituted in a strong correlation ($r = 0.99$) between Ga and Al in all samples (Figure 10a) [34,35]. Previous research indicates Ga in aluminum oxides (e.g., boehmite, gibbsite, and diaspore) in bauxite ore [32,34–36]. Due to the ease with which the float-sink method separated diaspores from density-fractionated samples, correlation analysis ($r = 0.93$) revealed that Ga was mainly associated with diaspores in the study (Figure 9c).

Previous studies have shown that the occurrence of V in bauxite mainly occurs in titanium oxides [35,37]. V could be used as an isomorphous alternative for Ti in Ti-bearing materials due to their similar ionic radius. XRD analysis indicates that the Ti-bearing minerals in the bauxite samples are mainly anatase (Table 1, Figure 2a). Using μXRF analysis, Ti and V elemental mapping revealed a similar spatial distribution for both elements (Figure 11). In particular, the elemental distribution of granular Ti, most likely anatase, was highly consistent with that of V, implying that anatase is the main carrier

mineral for V. This is supported by the positive correlation ($r = 0.98$) between TiO_2 and V in all samples excluding the $>2.65 \text{ g/cm}^3$ density fractions (Figure 10b). Figure 10b also indicates that additional V occurs in other materials as suggested by the three outliers from the $>2.65 \text{ g/cm}^3$ density-fractionated samples that are beyond the trend line. Therefore, the modes of occurrence of V in these samples were diverse, but anatase was the primary host mineral of V.

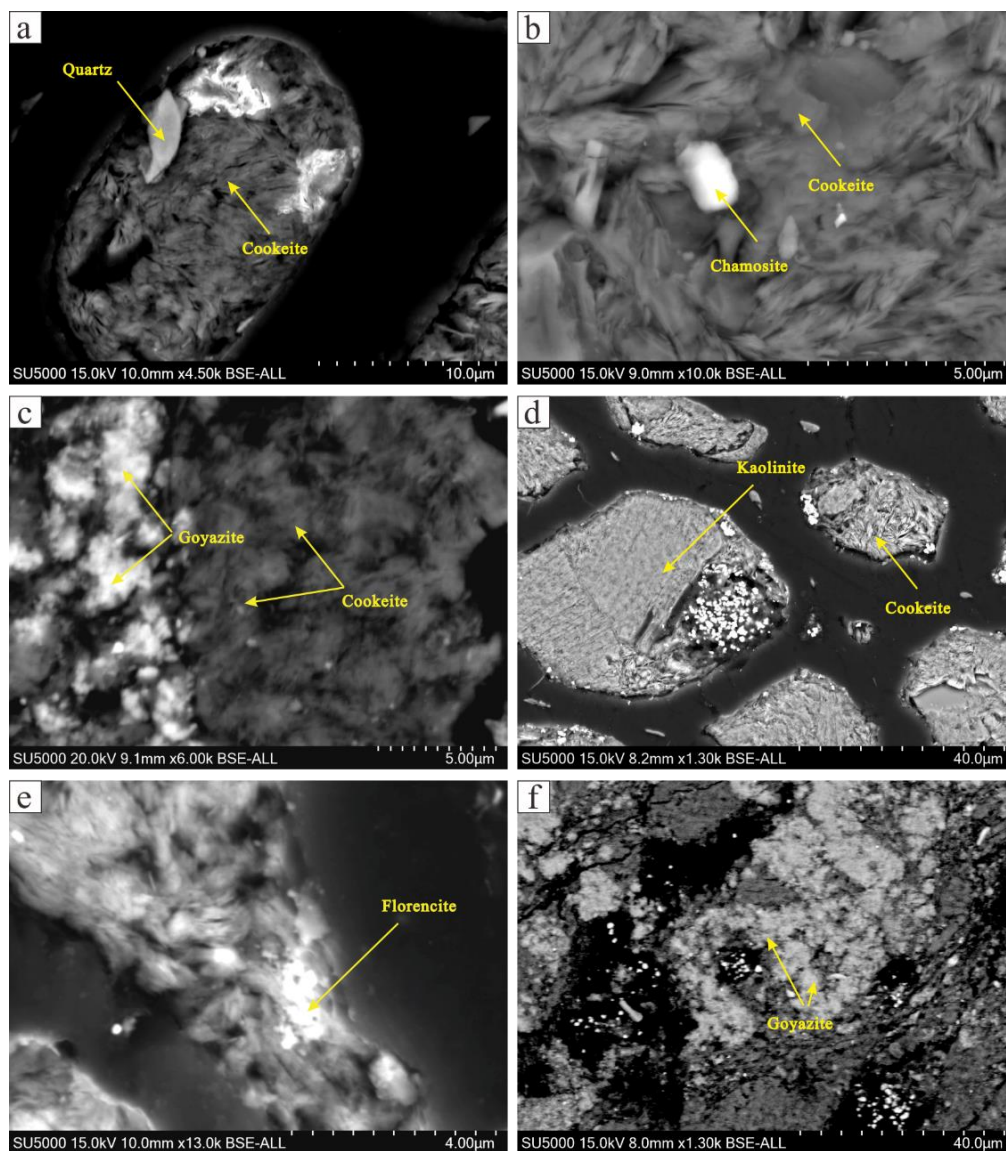


Figure 8. SEM back-scattered images of minerals in the sample. coexisting cookeite and quartz in cell-infilling (a); pillar-like chamosite in the cookeite (b); coexisting cookeite and goyazite (c); cookeite and kaolinite in cell-infillings (d); florencite in the clay matrix (e); goyazite in kaolinite matrix (f). EDS data are as in Supplementary Table S2.

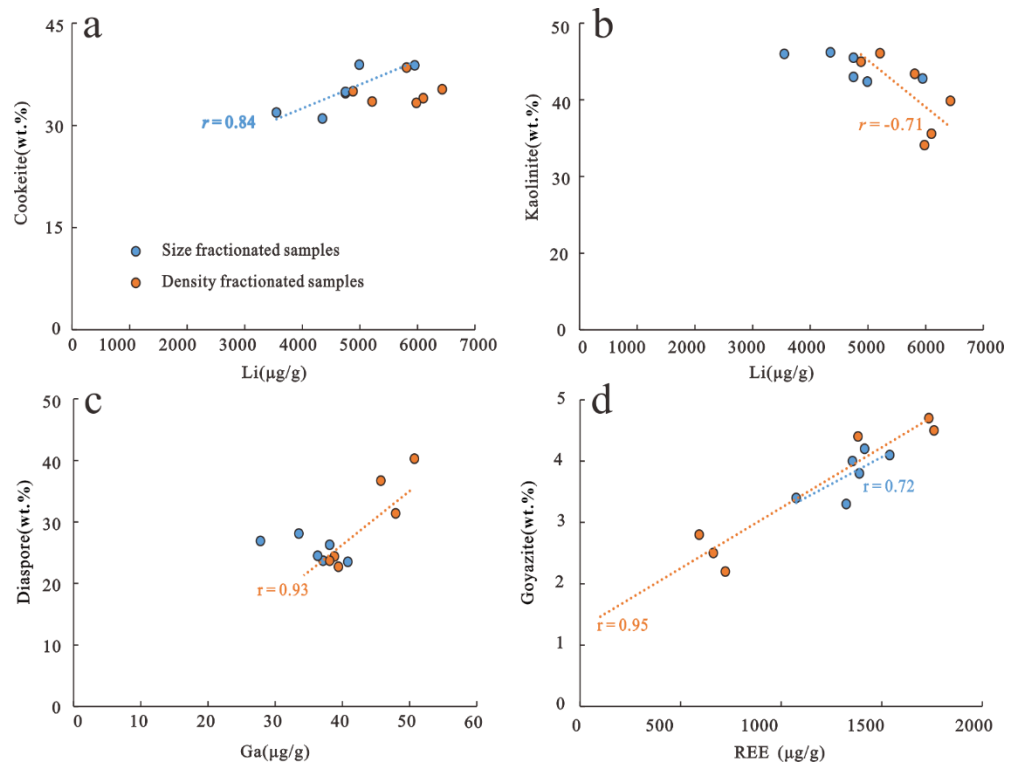


Figure 9. Relationship of Li vs. Cookeite (a), Li vs. Kaolinite (b), Ga vs. Diaspore (c), REE vs. Goyazite (d) in the low-grade bauxite samples subjected to size and density fractionation.

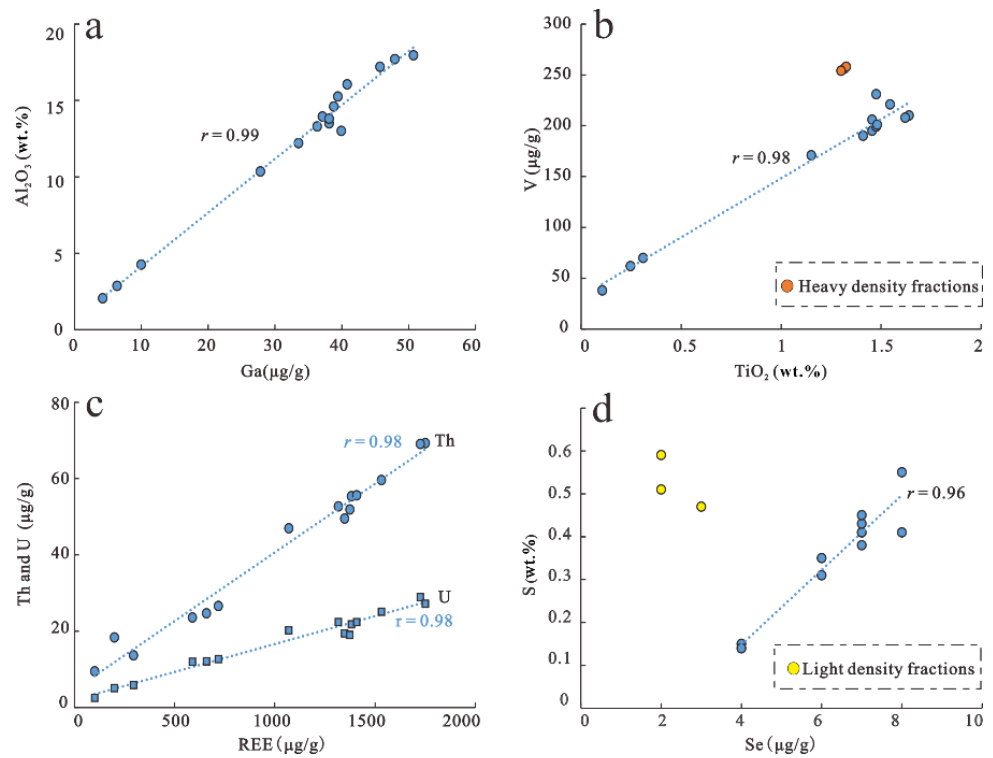


Figure 10. Bivariate plots of Ga vs. Al_2O_3 (a), TiO_2 vs. V (b), REE vs. Th and U (c), and Se vs. S (d). All the data are from size and density fractionated samples.

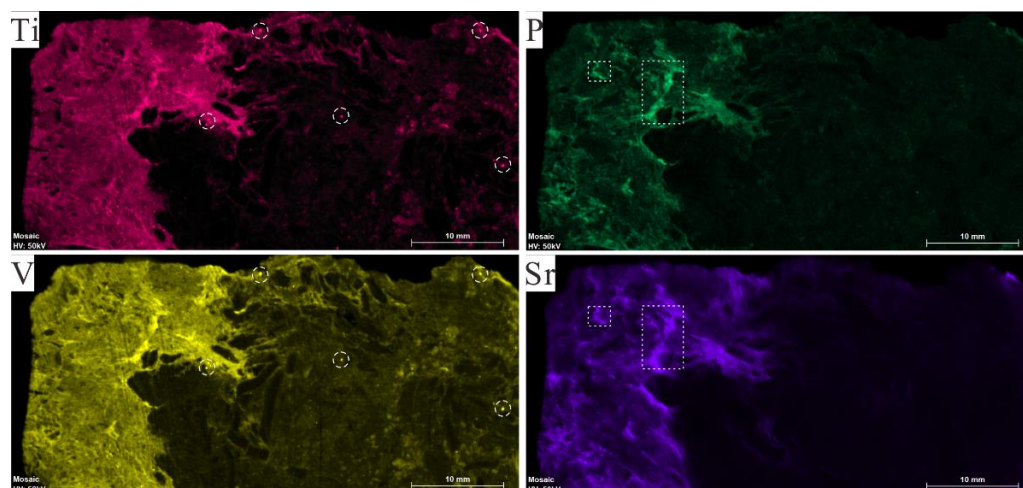


Figure 11. Elemental maps of Ti, V, P, and Sr in the sample Y1 obtained by the scanning μ XRF mapping technique. The circular boxes represent the highly overlapping areas of the elements Ti and V; the rectangular boxes represent the highly overlapping areas of the elements P and Sr.

4.3. Modes of Occurrence of REEs in Low-Grade Bauxite

Critical metal REEs are irreplaceable raw materials for high-tech and military industries, and their significance can no longer be measured in terms of a single economic value. Because of the scarcity of REE resources in European and other countries, many researchers attribute great importance to the REE resources in bauxite and bauxite residues [4,8]. Many REE-rich apatite and REE-independent minerals have been identified in karst bauxite in previous studies [10,38–40]. In this study, the total rare earth oxide (TREO) content of 0.15 wt% in sample Y1 is higher than the marginal grade in weathering crust-type REE deposits ($\text{TREO} \geq 0.1\%$; [41]). Among the size-fractionated samples, sample L3 with a particle size of $-0.25 + 0.125$ mm had the highest REE content ($1539.25 \mu\text{g/g}$). The float-sink method shows that REEs were enriched in the middle density fractions, of which sample L2-2 had the highest REE content ($1759.59 \mu\text{g/g}$).

A small proportion of goyazite in the sample was discovered by XRD and SEM-EDS analysis (Table 1, Figure 8c,f), which is also confirmed by P and Smapping analysis (Figure 11). The positive correlation of REEs vs. goyazite in the size- and density-fractionated samples (Figure 9d) implies that goyazite was the primary host mineral of REEs. In addition to the REE-bearing goyazite, florencite was discovered by SEM-EDS (Figure 8e) as suggested by the P, Ce, and Al detected by EDS (Supplementary Table S2). Furthermore, Figure 10d demonstrates strong correlations between REEs and Th and U in all samples, implying that the radioactive elements U and Th were also controlled by goyazite.

4.4. Modes of Occurrence of Se in Low-Grade Bauxite

Se is an essential trace element for humans and animals, as well as an environmentally sensitive element with both toxic and beneficial biological functions [42–44]. High selenium concentrations are coupled with black shales and sulfide mineralization in coals, while Se concentrations in most other rock types are very low [42,45]. The maximum Se content in the Permian black-shale sequence in South China, for example, is $8390 \mu\text{g/g}$ [46], demonstrating that Se, as a distributed element, is not only exceedingly low in the UCC ($0.05 \mu\text{g/g}$), but also has an extremely uneven distribution. The Se content of the sample Y1 was 10 g/g . In size-fractionated samples, the variation in Se content was very small, ranging from $7\text{--}8 \mu\text{g/g}$. The Se content in the density-fractionated samples was enriched in the medium density fractions, ranging from $6\text{--}7 \mu\text{g/g}$ (Figure 4d).

The mode of occurrence of Se in bauxite has received little attention in the literature. Se in coal commonly occurs in sulfides and organic matter [6]. By using the neutron activation

technique, Zhao [47] found that the average Se content of pyrite in coal reached 34.1 $\mu\text{g/g}$. Because Se and S have very similar physicochemical properties, Se isomorphically occurs in sulfides. Based on selective leaching experiments, Wen et al. [48] estimated that 75 percent of the selenium in the Laerma Se-Au deposit in China is connected with organic matter, which is attributed to the substitution of Se for S in organic matter.

Although not in sufficient abundance to be detected by direct methods such as XRD, μXRF , and SEM-EDS, the modes of occurrence of Se in this study can still be investigated using a combination of float-sink experiments and correlation analysis (indirect methods). Except for the light density-fractionated samples ($<1.60\text{ g/cm}^3$), Se and S show a positive correlation ($r = 0.92$) in the rest of the samples (Figure 10). As mentioned previously, organic matter was abundant in the light density-fractionated samples and the elevated concentrations of S were closely associated with organic matter. However, Figure 10d shows that the Se contents were not elevated with S contents in the light density samples, suggesting that Se is not correlated with the S in organic matter. As a result, we deduce that Se in the low-grade bauxite primarily occurs in sulfides.

5. Conclusions

Although the southern Shanxi Province contains many mineable bauxite resources, the low-grade bauxite in this area has been underestimated for its potential industrial recovery of critical metal elements such as Li, Ga, V, Se, and REEs. In this study, the modes of occurrence of these critical metal elements were studied using a combination of direct and indirect analytical methods.

The results exhibited that Li in the low-grade bauxite was mainly hosted in cookeite as an independent mineral. Ga in the low-grade bauxite was mainly associated with diaspore. In the low-grade bauxite, anatase is the main carrier mineral for V. REEs were present in the low-grade bauxite in multiple modes of occurrence. The major host mineral is goyazite, and to a lesser extent, florencite. Se in the low-grade bauxite primarily occurs in sulfides. Furthermore, because environmentally sensitive elements such as Se are present, the use of these resources should be carefully examined in an integrated manner.

Supplementary Materials: The following supporting information can be downloaded at: <https://www.mdpi.com/article/10.3390/min12080990/s1>, Table S1: Major (wt.%) and trace element ($\mu\text{g/g}$) content of Low-Grade bauxite with different particle sizes and density grades; Table S2: Energy spectrum data (atoms %) of SEM in Figures 2 and 9.

Author Contributions: Conceptualization, S.Z. (Shangqing Zhang); formal analysis, J.L. and S.Z. (Shangqing Zhang); investigation, J.L., X.Z. and M.Z.; resources, D.L.; data curation, S.Z. (Shuang Zhao) and H.D.; writing—original draft, S.Z. (Shangqing Zhang), J.L. and X.Z.; writing—review and editing, S.Z. (Shangqing Zhang) and L.Z.; visualization, H.D.; supervision, D.L. and F.Z.; project administration, F.Z.; funding acquisition, L.Z., X.L. and D.L. All authors contributed to the article and approved the submitted version. All authors have read and agreed to the published version of the manuscript.

Funding: This research was jointly supported by the National Natural Science Foundation of China (No. 42022015 and No. 41972073) and Science and Technology Innovation Foundation of Shanxi Provincial Geological Prospecting Bureau, China (2020-07).

Data Availability Statement: All datasets generated for this study are included in the article/Supplementary Material, further inquiries can be directed to the corresponding author.

Conflicts of Interest: The authors declare no conflict of interest.

References

1. Trump, D. A Federal Strategy to Ensure Secure and Reliable Supplies of Critical Minerals. Donald Trump, Washington, DC, USA. Available online: <https://www.federalregister.gov/documents/2017/12/26/2017-27899/a-federal-strategy-to-ensure-secure-and-reliable-supplies-of-critical-minerals> (accessed on 3 April 2018).
2. European Commission. *A New Industrial Strategy for Europe. Communication from the Commission to the European Parliament, the Council, the European Economic and Social Committee and the Committee of the Regions, COM(2020) 102 Final*; European Commission: Brussels, Belgium, 2020.
3. Gulley, A.L.; Nassar, N.T.; Xun, S. China, the United States, and competition for resources that enable emerging technologies. *Proc. Natl. Acad. Sci. USA* **2018**, *115*, 4111–4115. [[CrossRef](#)]
4. Radusinović, S.; Papadopoulos, A. The potential for REE and associated critical metals in karstic bauxites and bauxite residue of Montenegro. *Minerals* **2021**, *11*, 975. [[CrossRef](#)]
5. Zhang, J.Y.; Ren, D.Y.; Zhao, F.H.; Xu, D.W. Research methods of occurrences of trace elements in coal. *Coal Convers.* **1998**, *21*, 12–17. (In Chinese with English Abstract)
6. Dai, S.F.; Finkelman, R.B.; French, D.; Hower, J.C.; Graham, I.T.; Zhao, F.H. Modes of occurrence of elements in coal: A critical evaluation. *Earth-Sci. Rev.* **2021**, *222*, 103815. [[CrossRef](#)]
7. Mordberg, L.E. Geochemical evolution of a Devonian diaspore–crandallite–svanbergite-bearing weathering profile in the Middle Timan, Russia. *J. Geochem. Explor.* **1999**, *66*, 353–361. [[CrossRef](#)]
8. Mongelli, G.; Boni, M.; Oggiano, G.; Mameli, P.; Rosa, S.; Roberto, B.; Mondillo, N. Critical metals distribution in Tethyan karst bauxite: The cretaceous Italian ores. *Ore Geol. Rev.* **2017**, *86*, 526–536. [[CrossRef](#)]
9. Zhang, Y.S.; Zhang, J. Study on the Occurrence State of Lithium in Low-Grade Diasporic Bauxite from Central Guizhou Province, China. *JOM* **2019**, *71*, 4594–4599. [[CrossRef](#)]
10. Liu, X.F.; Wang, Q.F.; Zhang, Q.Z.; Zhang, Y.; Li, Y. Genesis of REE minerals in the karstic bauxite in western Guangxi, China, and its constraints on the deposit formation conditions. *Ore Geol. Rev.* **2016**, *75*, 100–115. [[CrossRef](#)]
11. Zhu, K.Y.; Su, H.M.; Jiang, S.Y. Mineralogical control and characteristics of rare earth elements occurrence in Carboniferous bauxites from western Henan Province, north China: A XRD, SEM-EDS and LA-ICP-MS analysis. *Ore Geol. Rev.* **2019**, *114*, 103144. [[CrossRef](#)]
12. Vind, J.; Malfliet, A.; Bonomi, C.; Paiste, P.; Sajó, I.E.; Blanpain, B.; Tkaczyk, A.H.; Vassiliadou, V.; Panyas, D. Modes of occurrences of scandium in Greek bauxite and bauxite residue. *Miner. Eng.* **2018**, *123*, 35–48. [[CrossRef](#)]
13. Ling, K.Y.; Tang, H.S.; Zhang, Z.W.; Wen, H.J. Host minerals of Li–Ga–V–rare earth elements in Carboniferous karstic bauxites in southwest China. *Ore Geol. Rev.* **2020**, *119*, 103325. [[CrossRef](#)]
14. Zhang, S.Q.; Liu, X.F.; Zhao, F.H.; Liu, D.N.; Zou, Y.; Zhang, W.X.; Liu, X.L.; Li, L.; Zhao, L.H. Geological and geochemical characteristics of karst bauxite-bearing sequences in Xiabu area, Central Shanxi Province, North China. *J. Geochem. Explor.* **2021**, *230*, 106849. [[CrossRef](#)]
15. Chen, P.; Chai, D.H. *Sedimentary Geochemistry of Carboniferous Bauxite Deposits in Shanxi Massif*; Shanxi Science and Technology Press: Shanxi, China, 1997; pp. 1–194. (In Chinese)
16. GB/T 478-2008; National Standard of the P.R.China: Method for Float and Sink Analysis of Coal. Standardization Administration of China: Beijing, China, 2009.
17. Taylor, J.C. Computer Programs for Standardless Quantitative Analysis of Minerals Using the Full Powder Diffraction Profile. *Powder Diffr.* **1991**, *6*, 2–9. [[CrossRef](#)]
18. SY/T 5163-2018; Oil and Gas Industry Standard of the P.R.China: Analysis Method for Clay Minerals and Ordinary Non-Clay Minerals in Sedimentary Rocks by the X-Ray Diffraction. National Energy Administration: Beijing, China, 2019.
19. Franzini, M.; Leoni, L.; Saitta, M. A simple method to evaluate the matrix effects in X-Ray fluorescence analysis. *X-ray Spectrom.* **1972**, *1*, 151–154. [[CrossRef](#)]
20. Liang, Q.; Jing, H.; Gregoire, D.C. Determination of trace elements in granites by inductively coupled plasma mass spectrometry. *Talanta* **2000**, *51*, 507–513. [[CrossRef](#)]
21. Li, J.H.; Li, Q.L.; Zhao, L.; Zhang, J.H.; Tang, X.; Gu, L.X.; Guo, Q.; Ma, H.X.; Zhou, Q.; Liu, Y.; et al. Rapid screening of Zr-containing particles from Chang'e-5 Lunar soil samples for isotope geochronology: Technical roadmap for future study. *Geosci. Front.* **2022**, *13*, 101367. [[CrossRef](#)]
22. Dai, S.F.; Liu, J.J.; Ward, C.R.; Hower, J.C.; French, D.; Jia, S.H.; Hood, M.M.; Garrison, T.M. Mineralogical and geochemical compositions of Late Permian coals and host rocks from the Guxu Coalfield, Sichuan Province, China, with emphasis on enrichment of rare metals. *Int. J. Coal Geol.* **2016**, *166*, 71–95. [[CrossRef](#)]
23. DZ/T 0202-2020; Geology Mineral Industry Standard of PR China: Specifications for Bauxite Mineral Exploration. Ministry of Natural Resources of the People's Republic of China: Beijing, China, 2020.
24. Taylor, S.R.; McLennan, S.M. *The Continental Crust: Its Composition and Evolution*; Blackwell: Oxford, UK, 1985; p. 312.
25. Wen, H.J.; Luo, C.G.; Du, S.J.; Yu, W.X.; Gu, H.N.; Ling, K.Y.; Cui, Y.; Li, Y.; Yang, J.H. Carbonate-hosted clay-type lithium deposit and its prospecting significance. *Chin. Sci. Bull.* **2019**, *65*, 53–59. (In Chinese with English Abstract) [[CrossRef](#)]
26. Zhang, J.Y.; Wang, Q.f.; Liu, X.F.; Zhou, G.F.; Xu, H.P.; Zhu, Y.G. Provenance and ore-forming process of Permian lithium-rich bauxite in central Yunnan, SW China. *Ore Geol. Rev.* **2022**, *145*, 104862. [[CrossRef](#)]

27. Ling, K.Y.; Wen, H.Z.; Zhang, Q.Z.; Luo, C.G.; Gu, H.N.; Du, S.J.; Yu, W.X. Super-enrichment of lithium and niobium in the upper Permian Heshan Formation in Pingguo, Guangxi, China. *Sci. China Earth Sci.* **2021**, *64*, 753–772. [[CrossRef](#)]
28. Yang, S.J.; Wang, Q.F.; Deng, J.; Wang, Y.Z.; Kang, W.; Liu, X.F.; Li, Z.M. Genesis of karst bauxite-bearing sequences in Baofeng, Henan (China), and the distribution of critical metals. *Ore Geol. Rev.* **2019**, *115*, 103161. [[CrossRef](#)]
29. Bailey, S.W.; Lister, J.S. Structures, compositions, and X-ray diffraction identification of dioctahedral chlorites. *Clays Clay Miner.* **1989**, *37*, 193–202. [[CrossRef](#)]
30. Zhao, L.; Ward, C.R.; French, D.; Graham, I.T.; Dai, S.F.; Yang, C.; Xie, P.P.; Zhang, S.Y. Origin of a kaolinite-NH₄-illite-pyrophyllite-chlorite assemblage in a marine-influenced anthracite and associated strata from the Jincheng Coalfield, Qinshui Basin, Northern China. *Int. J. Coal Geol.* **2018**, *185*, 61–78. [[CrossRef](#)]
31. Calagari, A.A.; Abedini, A. Geochemical investigations on Permo-Triassic bauxite horizon at Kanisheeteh, east of Bukan, West-Azarbaidjan, Iran. *J. Geochem. Explor.* **2007**, *94*, 1–18. [[CrossRef](#)]
32. Haniłci, N. Geological and geochemical evolution of the Bolkardađı bauxite deposits, Karaman, Turkey: Transformation from shale to bauxite. *J. Geochem. Explor.* **2013**, *133*, 118–137. [[CrossRef](#)]
33. Zhao, T.; Qin, P.Z.; Wang, A.J.; Wang, G.S.; Li, J.W.; Liu, C.; Liu, Y.F. An analysis of gallium ore resources demand trend and the thinking concerning China’s gallium industry development. *Acta Geosci. Sin.* **2017**, *38*, 77–84, (In Chinese with English Abstract).
34. Mongelli, G.; Buccione, R.; Gueguen, E.; Langone, A.; Sinisi, R. Geochemistry of the Apulian allochthonous karst bauxite, Southern Italy: Distribution of critical elements and constraints on Late Cretaceous Peri-Tethyan palaeogeography. *Ore Geol. Rev.* **2016**, *77*, 246–259. [[CrossRef](#)]
35. Mongelli, G.; Boni, M.; Buccione, R.; Sinisi, R. Geochemistry of the Apulian karst bauxites (southern Italy): Chemical fractionation and parental affinities. *Ore Geol. Rev.* **2014**, *63*, 9–21. [[CrossRef](#)]
36. Liu, X.F.; Wang, Q.; Feng, Y.W.; Li, Z.M.; Cai, S.H. Genesis of the Guangou karstic bauxite deposit in western Henan, China. *Ore Geol. Rev.* **2013**, *55*, 162–175. [[CrossRef](#)]
37. Mordberg, L.E.; Stanley, C.J.; Germann, K. Mineralogy and geochemistry of trace elements in bauxites: The Devonian Schugorsk deposit, Russia. *Mineral. Mag.* **2001**, *65*, 81–101. [[CrossRef](#)]
38. Wang, Q.F.; Deng, J.; Liu, X.F.; Zhang, Q.Z.; Sun, S.L.; Jiang, C.Z.; Zhou, F. Discovery of the REE minerals and its geological significance in the Quyang bauxite deposit, West Guangxi, China. *J. Asian. Earth. Sci.* **2010**, *39*, 701–712. [[CrossRef](#)]
39. Ling, K.Y.; Zhu, X.Q.; Tang, H.S.; Du, S.J.; Gu, J. Geology and geochemistry of the Xiaoshanba bauxite deposit, Central Guizhou Province, SW China: Implications for the behavior of trace and rare earth elements. *J. Geochem. Explor.* **2018**, *190*, 170–186. [[CrossRef](#)]
40. Laskou, M.; Andreou, G. Rare earth elements distribution and REE-minerals from the Parnassos–Ghiona bauxite deposits, Greece. In Proceedings of the Mineral Exploration and Sustainable Development, 7th Biennial SGA Meeting, Athens, Greece, 24–28 August 2003.
41. DZ/T 0203-2020; Geology Mineral Industry Standard of P.R. China: Specifications for Rare Metal Mineral Exploration. Ministry of Natural Resources of the People’s Republic of China: Beijing, China, 2020.
42. Fordyce, F.M. Selenium deficiency and toxicity in the environment. In *Essentials of Medical Geology*; Springer: Dordrecht, The Netherlands, 2013; pp. 375–416.
43. Dhillon, K.S.; Dhillon, S.K.; Bijay, S. Chapter One—Genesis of seleniferous soils and associated animal and human health problems. In *Advances in Agronomy*; Sparks, D.L., Ed.; Academic Press: Cambridge, MA, USA, 2019; Volume 154, pp. 1–80.
44. Dhillon, K.S.; Dhillon, S.K. Development and mapping of seleniferous soils in northwestern India. *Chemosphere* **2014**, *99*, 56–63. [[CrossRef](#)] [[PubMed](#)]
45. Long, J.; Luo, K.L. Trace element distribution and enrichment patterns of Ediacaran-early Cambrian, Ziyang selenosis area, Central China: Constraints for the origin of Selenium. *J. Geochem. Explor.* **2017**, *172*, 211–230. [[CrossRef](#)]
46. Song, C.Z. A brief description of the Yutangba sedimentary type selenium mineralized area in southwestern Hubei. *Miner. Depos.* **1989**, *8*, 83–89.
47. Zhao, F.H. Study on the Mechanism of Distributions and Occurrences of Hazardous Minor and Trace Elements in Coal and Leaching Experiments of Coal Combustion Residues. Ph.D. Thesis, China University of Mining & Technology-Beijing, Beijing, China, 1997.
48. Wen, H.J.; Qiu, Y.Z. Organic and inorganic occurrence of selenium in Laerma Se-Au deposit. *Sci. China Ser. D Earth Sci.* **1999**, *42*, 662–669. [[CrossRef](#)]